

Data Analysis of the Drell-Yan Process in the CMS Experiment at the LHC

A Third-Semester Dissertation Submitted to
Department of Physics and Astrophysics
University of Delhi, Delhi-110007



in Partial Fulfillment of the Requirements for the Degree of
Master of Science in Physics

by

Anuj Raghav

M.Sc. Physics, 3rd Semester, Group - F4

University Roll No: 23222762018

under the supervision of

Dr. Arun Kumar

December, 2024

Undertaking

This dissertation is submitted in partial fulfillment of the requirements for the Master of Science degree in Physics and was conducted under the supervision of Dr. Arun Kumar.

I declare that this dissertation has been composed solely by myself and is free from any form of plagiarism. Except where otherwise indicated by reference or acknowledgment, all work presented here is entirely my own.



Anuj Raghav
(Candidate)



Dr. Arun Kumar
(Supervisor)

Abstract

The study of fundamental particles requires the identification and properties of various particles. Accurate particle detection relies on understanding their interactions with matter, which is achieved through advanced particle detectors. The Compact Muon Solenoid (CMS) is one such particle detector at the heart of the Large Hadron Collider (LHC), located at the European Organization for Nuclear Research (CERN), Geneva, Switzerland.

This study focuses on the qualitative analysis of the Drell-Yan process via the production of a Z -boson in the intermediate mass range ($60 \text{ GeV} < M_Z < 120 \text{ GeV}$), decaying into an electron-positron pair ($Z \rightarrow e^+e^-$). Like any other physical process, this one also involves unwanted background contributions. The primary objective is to identify the Drell-Yan signal and distinguish it from these background processes that can mimic the Drell-Yan signature.

The study is divided into two phases. During the current semester, the focus is on understanding the Drell-Yan process ($q\bar{q} \rightarrow Z \rightarrow e^+e^-$) in the context of the CMS experiment at the LHC. Additionally, the study examines how various background processes can introduce deviations from the predicted results. In the subsequent semester, the emphasis will shift to developing and implementing techniques to effectively suppress these backgrounds.

The analysis is based on publicly available data from the CERN open data which takes the Monte Carlo (MC) sample corresponds to the DYJetsToLL_M-50-LO process, which simulates Drell-Yan (DY) production of lepton-antilepton pairs ($\ell^+\ell^-$) with an invariant mass greater than 50 GeV.

Acknowledgment

I extend my deepest gratitude to my supervisor, Dr. Arun Kumar, Assistant Professor, Department of Physics and Astrophysics, University of Delhi, for his positive attitude, constructive guidance, and unwavering support throughout the course of this dissertation. His dedication and passion for High Energy Physics have been a continuous source of motivation throughout this journey.

I would also like to express my heartfelt thanks to Prof. Kirti Ranjan, Professor, Department of Physics and Astrophysics, University of Delhi, for his invaluable experience and insights, which have greatly inspired me to pursue this field.

Additionally, I am deeply grateful to Prof. Debajyoti Choudhury, Head of the Department, Department of Physics and Astrophysics, for fostering a supportive academic environment and for his encouragement during this academic pursuit.

Lastly, I would like to thank the department and library staff for providing a conducive atmosphere and essential resources that have been instrumental in shaping my understanding and research in High Energy Physics.

Contents

Undertaking	iv
Abstract	vi
Acknowledgments	viii
1 Theoretical Groundwork	13
1.1 Interaction of Radiation with Matter	13
1.1.1 Interaction of Heavy Charged Particles with Matter	13
1.1.2 Interaction of Fast Electrons with Matter	15
1.1.3 Interaction of Photons with Matter	16
1.2 Drell-Yan process	18
1.2.1 Z boson	19
1.2.2 Z production in the Drell-Yan process	19
2 The CMS Experiment	21
2.1 Large Hadron Collider	21
2.2 The Compact Muon Solenoid	23
2.2.1 Terminology	24
2.2.2 The Superconducting Magnet	25
2.2.3 Inner Tracker	26
2.2.4 Energy Measurement	27
2.2.5 Muon System	28
2.3 Electromagnetic Calorimeter	28
2.3.1 Physics of the Electromagnetic Shower	29
2.3.2 Energy resolution of Electromagnetic Calorimeter	31
2.4 Electron Reconstruction and Identification	32
2.4.1 Electron Clustering and Superclustering	32
2.4.2 Track Reconstruction	32
2.4.3 Electron Identification	33

3	Data Analysis	35
3.1	Data Acquisition	35
3.2	Selection Criteria	36
3.3	Drell-Yan ($Z \rightarrow e^+e^-$) Plots	37
3.4	Plots with Backgrounds	42
4	Conclusion	45
	Bibliography	47

List of Figures

1.1	Mean energy loss rate in liquid hydrogen, gaseous helium, carbon, aluminum, iron, tin, and lead.	14
1.2	Emission of <i>Bremsstrahlung</i> radiation	16
1.3	The lower curve shows, as a function of the atomic number Z of the target material, the photon energy E below which photoelectric absorption is the most probable interaction mechanism, while the upper curve shows the energy above which pair production is the most important process. The shaded region between the two curves corresponds to the domain where Compton scattering dominates. The cross sections are taken from the NIST XCOM database.	17
1.4	The Feynman diagram of the Drell-Yan process	18
2.1	Aerial view of LHC complex	21
2.2	The top view of CMS detector	23
2.3	The transverse view of the CMS.	24
2.4	Coordinate system of the CMS.	25
2.5	(a) Fractional energy lost in lead by electrons and positrons as a function of energy. (b) Photon interaction cross-section in lead as a function of energy.	29
2.6	(a) and (b) show electron and photon showers respectively in the ECAL	31
3.1	Transverse momentum of leading and trailing electron after passing the selection cuts.	39
3.2	Pseudorapidity of leading and trailing electron after passing the selection cuts.	40
3.3	Plots for the $M_{\ell\ell}$, $p_{T\ell\ell}$, $\Delta\phi_{\ell\ell}$, and Missing transverse energy for the Drell-Yan signal. The calculation of these quantities are shown above.	41

3.4	Plots for the $p_{T\ell\ell}$, $\Delta\phi_{\ell\ell}$, and Missing transverse energy for the Drell-Yan signal along with the pre-mentioned backgrounds. This analysis is based on setting a cut on invariant mass, $60 < M_{\ell\ell} < 120$. . .	42
3.5	Comparison of invariant mass, $M_{\ell\ell}$, of the lepton pair with (left) and without (right) cuts applied.	43

Chapter 1

Theoretical Groundwork

1.1 Interaction of Radiation with Matter

The detection of any particle (radiation) is usually based on its interactions with the matter of the detector medium[1].

To organize this discussion it is important to arrange the four major categories of radiation as[2] :

Charged Particulate Radiations	\leftrightarrow	Uncharged Radiations
Heavy charged particles		Neutrons
Fast electrons		X-rays and γ rays

Table 1.1: Categorization of different types of radiations

The entries in the left column represent charged particulate radiations, which interact primarily through Coulomb interactions due to the charge carried by the particle. The radiations in the right are uncharged and thus are not subjected to Coulomb interactions.

In this text our main focus will lie on the interaction of electrons, however brief accounts of others are also given.

1.1.1 Interaction of Heavy Charged Particles with Matter

A charged particle can lose energy in two ways while passing through any medium.

- Through ionization and excitation.
- *Bremsstrahlung*

We shall start our discussion with the coulombic interactions of charged particles. When a charged particle enters an absorbing medium, it simultaneously interacts with numerous electrons. In each interaction, the electron experiences an impulse from the particle's attractive Coulomb force as it passes nearby. The strength of this impulse depends on the encounter's proximity; in close encounters, the impulse may provide enough energy to either excite the electron to a higher shell within the absorber atom or completely remove the electron, causing ionization. The energy transferred to the electron is taken from the charged particle, which reduces the particle's velocity. For a single collision, the maximum energy transferable from a charged particle of mass m with kinetic energy E to an electron of mass m_0 is $\frac{4Em_0}{m}$, approximately 1/500 of the particle's energy per nucleon. Many such interactions cause the charged particle to lose almost their entire energy in this process.

The energy loss by this process is given by[3]

$$-\frac{dE}{dx} = \frac{4\pi e^4 z^2}{m_0 v^2} N Z \left[\ln \left(\frac{2m_0 v^2}{I} \right) - \ln \left(1 - \frac{v^2}{c^2} \right) - \frac{v^2}{c^2} \right] \quad (1.1)$$

Where ze is the charge of the particle, m_0 is the mass of the electron, N and Z are the number density and atomic number of the absorber atoms.

The reason why heavy charged particles do not show significant bremsstrahlung is discussed in the next section.

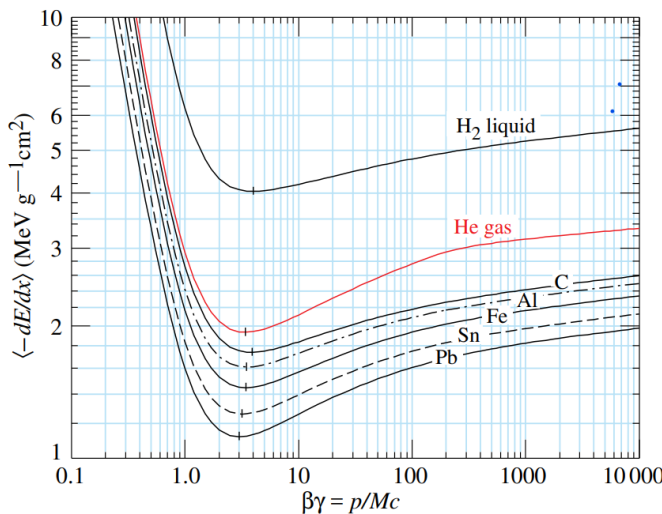


Figure 1.1: Mean energy loss rate in liquid hydrogen, gaseous helium, carbon, aluminum, iron, tin, and lead.[4]

1.1.2 Interaction of Fast Electrons with Matter

Like heavy charged particles, electrons (positrons) also suffer collisional energy when passing through an absorber material. However, this time the *bremsstrahlung* losses become more significant. At energies of few MeV or less, this process is still less. However, as the energy is increased to the 10's of MeV, loss due to bremsstrahlung becomes major as compared to collisional (ionization and excitation).

Therefore, the total energy lost in the case of fast electrons electron can be written as

$$\frac{dE}{dx} = \left(\frac{dE}{dx} \right)_{\text{collisional}} + \left(\frac{dE}{dx} \right)_{\text{radiative}} \quad (1.2)$$

Collisional Energy loss

The collisional loss for fast electrons is given by[5]:

$$-\left(\frac{dE}{dx} \right)_c = \frac{2\pi e^4}{m_0 v^2} N Z \left(\ln \left(\frac{m_0 v^2 E}{2I^2(1 - \beta^2)} \right) - (\ln 2) \left(2\sqrt{1 - \beta^2} - 1 + \beta^2 \right) + (1 - \beta^2) + \frac{1}{8} \left(1 - \sqrt{1 - \beta^2} \right)^2 \right). \quad (1.3)$$

where all the symbols have their usual meanings and $\beta \equiv v/c$.

Bremsstrahlung

In classical electrodynamics, an accelerated electron in the static field of the nucleus emits electromagnetic radiation, this radiation is termed *bremsstrahlung*. When a continuous and mono-energetic beam of electrons is made to interact with a thick or thin absorber the electron beam gets scattered due to the coulombic force between the positively charged heavy nucleus and the surrounding atomic electrons of the target atom. In this process, the projectile electron losses continuously a finite kinetic energy transformed into the emission of radiation see Figure 1.2. This transformed radiation is referred to as '*bremsstrahlung*' also known as 'braking radiation' or 'continuous radiation'.

This fraction of energy converted into *bremsstrahlung* increases with increasing electron energy and is greater for media of high atomic number. The acceleration produced by a nucleus of charge Ze on an incident particle ze and mass M is proportional to Zz^2/M . The intensity of *bremsstrahlung* radiation emitted is proportional to $(ze \times \text{acceleration})^2$ [6] [7].

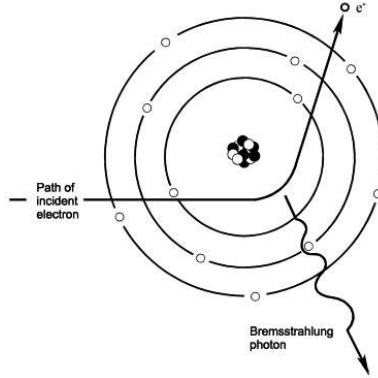


Figure 1.2: Emission of *Bremsstrahlung* radiation

The $(Z/M)^2$ dependence shows that *bremsstrahlung* is more important in a high Z medium and it is more important for electrons(positrons) than heavy charged particles.

Thus, the final expression for radiative energy loss through bremsstrahlung is given by[8]

$$-\left(\frac{dE}{dx}\right)_r = \frac{NEZ^2e^4}{137M^2c^4} \left(4 \ln \frac{2E}{Mc^2} - \frac{4}{3}\right) \quad (1.4)$$

1.1.3 Interaction of Photons with Matter

Photons (X-rays and γ - rays) interact with the matter via a range of mechanisms, which can be classified to the energy of the incoming radiation. As illustrated in the Figure 1.3, photo-absorption (photoelectric effect) constitutes the largest contribution to the total cross-section at low photon energies, pair production is the most frequent interaction at high energies, and Compton scattering dominates in the intermediate energy range.[9]

Photoabsorption

In Photo-absorption or as we know it photoelectric effect, a photon or gamma ray undergoes an interaction with an atom of the absorber medium causing the photon to completely disappear and leaving an energetic *photoelectron* from one of the bound shells of the atom. For photons (gamma rays) of sufficient energy, the photoelectron originates from the most tightly bound shell of the atom, which in most cases is *K* shell.

The photoelectron appears with energy given by

$$E_e = h\nu - \phi_0 \quad (1.5)$$

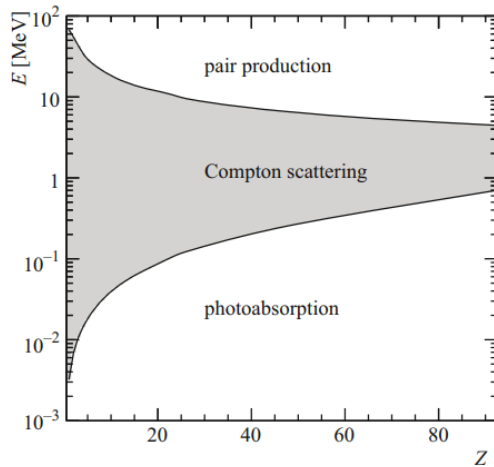


Figure 1.3: The lower curve shows, as a function of the atomic number Z of the target material, the photon energy E below which photoelectric absorption is the most probable interaction mechanism, while the upper curve shows the energy above which pair production is the most important process. The shaded region between the two curves corresponds to the domain where Compton scattering dominates. The cross sections are taken from the NIST XCOM database.[10]

where E_e is the kinetic of the photoelectron, $h\nu$ is the energy of the incoming photon and ϕ_0 is the binding energy of the photoelectron in its shell.

In addition, the gamma-ray can also create an ionized atom with a vacancy in one of the bound shells. This vacancy is promptly filled by capturing a free electron from the surrounding medium or by rearrangement from other atomic shells. As a result, one or more characteristic X-ray photons may be emitted. However, these X-rays are often reabsorbed near their point of origin, primarily through photoelectric absorption in less tightly bound electron shells.

Compton scattering

In Compton scattering, an incident gamma-ray photon is deflected by an angle θ from its original trajectory. This interaction transfers a portion of the photon's energy to an electron, initially considered to be at rest, which is then termed a recoil electron.

The energy of the scattered electron can be written as

$$E' = \frac{E}{1 + \frac{h\nu}{m_0 c^2} (1 - \cos\theta)} \quad (1.6)$$

where m_0 is the rest mass energy of the electron.

Pair Production

If the energy of the photon (gamma-ray) is more than twice the rest-mass energy of the electron, the interaction is dominated by pair production.

This interaction takes place in the Coulomb field of a nucleus, a gamma-ray photon is absorbed and transformed into an electron-positron pair. Any energy of the photon exceeding the 1.022 MeV (twice the rest mass energy of the electron) threshold required for this process is converted into kinetic energy of the electron-positron pair. As the positron slows down in the detector medium, it typically undergoes annihilation, producing two secondary annihilation photons.

1.2 Drell-Yan process

The Drell-Yan process is a fundamental mechanism in high-energy particle physics, describes the lepton pair production in hadron-hadron collisions, and was first suggested by Sidney D. Drell and Tung-Mow Yan in 1970. [11]

The quarks annihilate into a Z boson which then decays into a lepton pair as shown in Figure 1.4

$$q\bar{q} \rightarrow Z \rightarrow e^+e^-$$

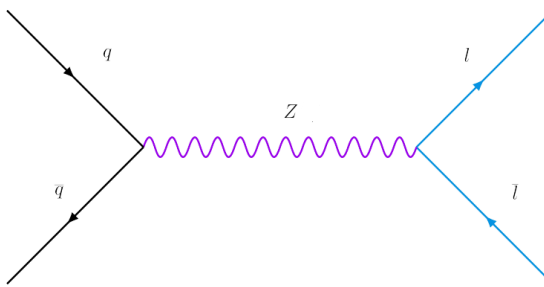


Figure 1.4: The Feynman diagram of the Drell-Yan process

As M_{ll} approaches M_Z , the Z boson production resonance starts to interfere with the lepton pair production and quickly becomes dominant. The Drell-Yan process is, in fact, the main mechanism for the production of the Z boson at the LHC.

In this study, our main focus will lie on the intermediate-mass region (60-120 GeV) to study the Drell-Yan through the Z boson as a mediator.

1.2.1 Z boson

A major breakthrough that highlighted the success of the Standard Model was the discovery of *the weak neutral current* or Z bosons in 1983 at UA1 collaboration, CERN [12]. This finding was particularly significant as it precisely aligned with the predictions made by Glashow, Weinberg, and Salam.

In later years more sophisticated experiments at LEP and the Tevatron measured the properties of the Z boson very precisely[13].

$$M_z = (91.1876 \pm 0.0021) \text{ GeV}$$

$$\Gamma_z = (2.4952 \pm 0.0023) \text{ GeV}$$

Precision tests of the Z boson decays into various lepton and quark pairs also confirmed that there are exactly three generations of light neutrinos, another key prediction of the Standard Model. The table shows the decay mode of Z bosons.

	Mode	Fraction (Γ_i/Γ)
Γ_1	e^+e^-	$(3.363 \pm 0.004) \%$
Γ_2	$\mu^+\mu^-$	$(3.366 \pm 0.007) \%$
Γ_3	$\tau^+\tau^-$	$(3.367 \pm 0.008) \%$
Γ_4	hadrons	$(69.91 \pm 0.06) \%$
Γ_5	invisible	$(20.00 \pm 0.06) \%$

1.2.2 Z production in the Drell-Yan process

The invariant mass¹ squared Q^2 of the dilepton system, as expressed in the Drell-Yan process, is given by:

$$Q^2 = x_1 x_2 s \quad (1.7)$$

This relation reflects the energy available for producing a high-mass dilepton pair in hadron-hadron collisions, with each variable holding a specific significance:

- s represents the square of the center-of-mass energy of the colliding hadrons. This value indicates the maximum energy accessible for any interaction occurring between partons within these hadrons.
- x_1 and x_2 denote the fractions of the longitudinal momenta carried by each of the interacting partons from the two colliding hadrons. These fractions

¹The invariant or dilepton mass is given by $M_{\ell\ell} = \sqrt{(E_1 + E_2)^2 - (\vec{p}_1 + \vec{p}_2)^2}$

fall within the range $0 < x_1, x_2 < 1$. Larger values of x_1 and x_2 imply that the parton carries a higher proportion of the hadron's total momentum.

In hadronic collisions, the Drell-Yan process produces a high-mass dilepton system (e.g., a muon or electron pair) through the interaction of partons (quarks or antiquarks) from each hadron. Since only a fraction of the hadrons' total momentum contributes to this partonic interaction, the effective energy available to produce the dilepton pair is less than the total energy s of the colliding hadrons. Instead, it depends on the longitudinal momentum fractions x_1 and x_2 of the colliding partons.

Thus, the product $x_1 x_2 s$ represents the partonic center-of-mass energy squared, which directly corresponds to the invariant mass squared Q^2 of the intermediate state in the Drell-Yan process. The invariant mass Q is then the actual mass of the Z boson mediating the dilepton production. At the LHC, the Z production is dominated by the Drell-Yan process see Figure 1.4, with the subsequent decay into a lepton-antilepton pair:

$$q\bar{q} \longrightarrow Z \longrightarrow \ell\bar{\ell}$$

The Drell-Yan production of a Z boson, followed by its decay into a lepton-antilepton pair ($\ell^+ \ell^-$), provides an invaluable reference for analysis in both the electron and muon channels. The decay produces a distinct and isolated lepton signature, facilitating precise calibration and performance evaluation within the detector.

Chapter 2

The CMS Experiment

In this chapter, the experimental setups involved in the process are described. The collider complex is briefly introduced and the description of the particle detector will be followed with details on its subsystem focusing primarily on the electron calorimeter. At last, triggers and electron reconstruction and identification.

2.1 Large Hadron Collider

The Large Hadron Collider (LHC) is the largest and most powerful accelerator and collider with a 26.7 km circumference located underground near Geneva across the border of Switzerland and France, associated with the European Organisation for Nuclear Research (CERN)[14]. It has been designed primarily to collide protons and lead ions. The choice of having a proton-proton collider as opposed to an electron-positron collider is motivated by the goal of reaching a very high energy scale with minimal synchrotron radiation losses[15]. These losses scale inversely with the fourth power of the particle mass, making proton collisions significantly more efficient for high-energy physics applications.



Figure 2.1: Aerial view of LHC complex[16]

It was designed to operate at a center of mass energy (\sqrt{s}) of 14TeV and the instantaneous luminosity of $10^{34} cm^{-2}s^{-1}$.

Here, the instantaneous luminosity \mathcal{L} represents the number of collisions in the collider per unit area (cm^2) and second. Hence, the number of events(collision) per second for any process can be expressed as:

$$\frac{dN_{event}}{dt} = \mathcal{L} \cdot \sigma_{process} \quad (2.1)$$

where, $\sigma_{process}$ is the cross-section of the process.

Therefore, \mathcal{L} is a measure of how much data can be produced by the machine. \mathcal{L} of a machine is determined by the formula[17]:

$$\mathcal{L} = \frac{N_b^2 n_b f_{rev} \gamma_r}{4\pi \epsilon_n \beta^*} F \quad (2.2)$$

The numerator is related to the number of collisions.

- N_b is the number of particles per bunch.
- n_b is the number of bunches in the beam.
- Hence, total particles are $N_b \times n_b$.
- f_{rev} is the revolution frequency.¹
- γ_r is the relativistic Lorentz vector.
- F is the reduction factor due to the crossing angle.

The denominator gives us the characteristics of the beam:

- ϵ_n , normalized transverse emittance that describes the average spread of the particle in the position-momentum phase space.
- The low ϵ_n means, the beam is confined in a small area with similar momentum, which leads to higher luminosity.
- β^* is the beta function at the interaction point which is the distance from the IP to the point where the width of the beam becomes twice the width at the IP. Low β^* has a more squeezed and concentrated shape which leads to higher luminosity.

¹ $f = \frac{\text{speed of proton}}{\text{circumference of LHC}}$

2.2 The Compact Muon Solenoid

The CMS detector is a multi-purpose particle detector designed to support a broad range of physics research, including Standard Model studies to the search for new Beyond Standard Model (BSM) physics and precision measurement of already known physics at the TeV scale are also the main highlights of the LHC physics program. It is located at one of the LHC's interaction points, known as Point 5, in an underground cavern near Cessy. The detector measures 28.7 meters in length, with a diameter of 15 meters, and weighs approximately 14,000 tons.

The central component of CMS is a large superconducting solenoid that produces a magnetic field of 3.8 T. Inside this solenoid, the innermost layer houses a silicon pixel and strip detector positioned close to the interaction point. Following this are an electromagnetic calorimeter, made of lead tungstate crystals a hadron calorimeter, and a Muon detector. The overall layout of the CMS detector is shown in Figure 2.2 and in Figure 2.3 and described in further sections.

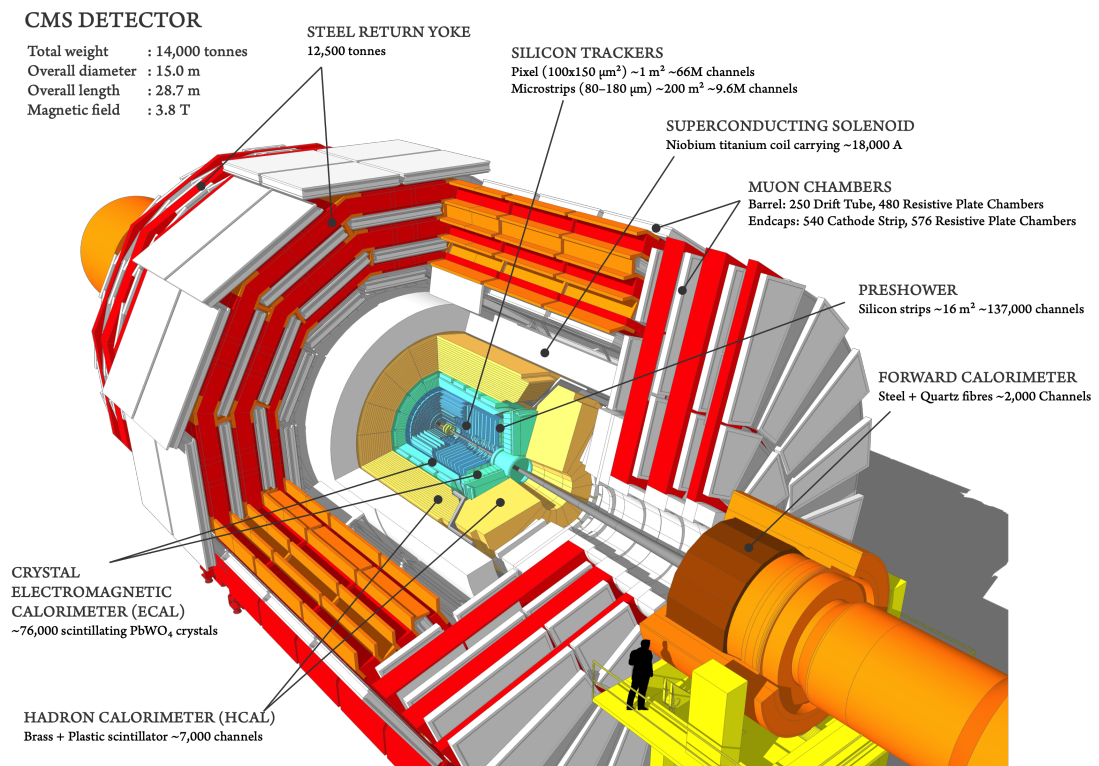


Figure 2.2: The top view of the CMS detector. [18]

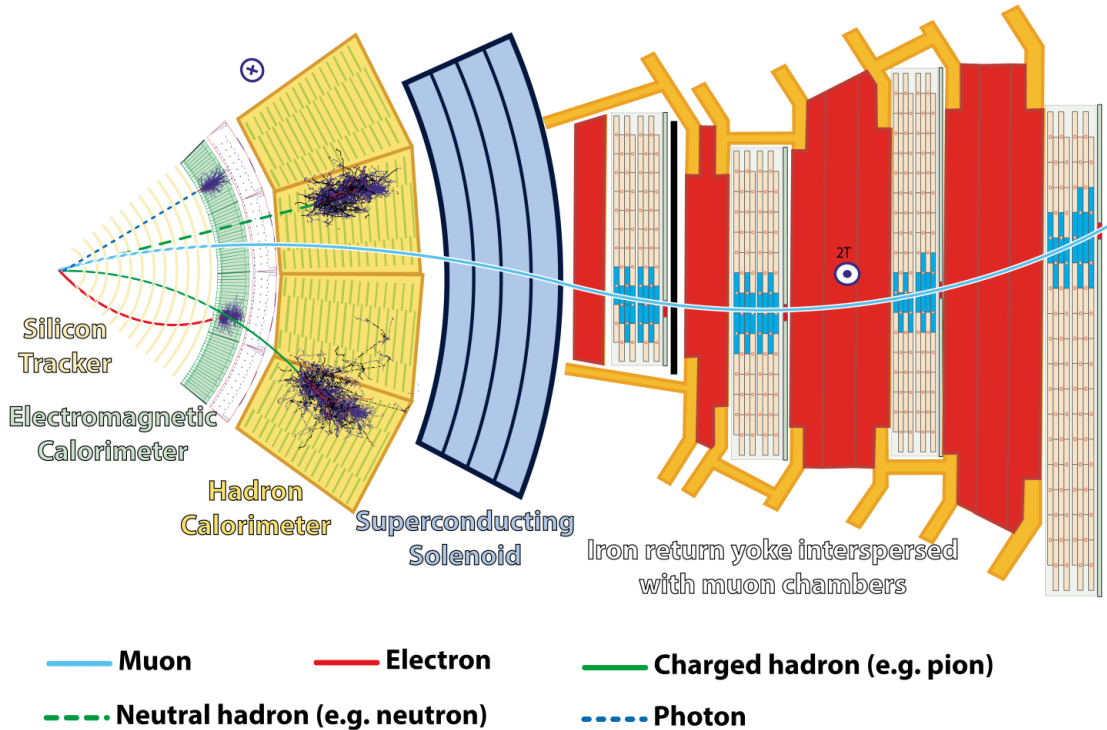


Figure 2.3: The transverse view of the CMS. [19]

2.2.1 Terminology

This section introduces some general terms and coordinate systems used for the detector [20]. The reference frame used is the standard CMS reference frame, a Cartesian system centered at the interaction point with the z -axis pointing along the beam direction towards the Tuna mountain from LHC point 5. The x -axis is chosen to be radially inwards towards the center of the LHC, and the y -axis is vertical and points upwards. In spherical polar coordinates, the coordinate system can be transformed to the polar angle θ (measured from the x -axis in the $x - y$ plane), the azimuthal angle ϕ (measured from the z -axis) and r the radial coordinate in the $x - y$ plane as shown in Figure 2.4.

The direction of the z -axis, i.e., the direction of the beam is referred to as *longitudinal*. The $x - y$ plane orthogonal to the beam is called *transverse* plane. Based on this, the momentum of a particle can be divided into two components: the *longitudinal momentum* p_z and the *transverse momentum* p_T , defined as

$$p_T = \sqrt{p_x^2 + p_y^2} \quad (2.3)$$

The rapidity (y) of a particle with energy E can be written as

$$y = \frac{1}{2} \ln \frac{E + p_z}{E - p_z} \quad (2.4)$$

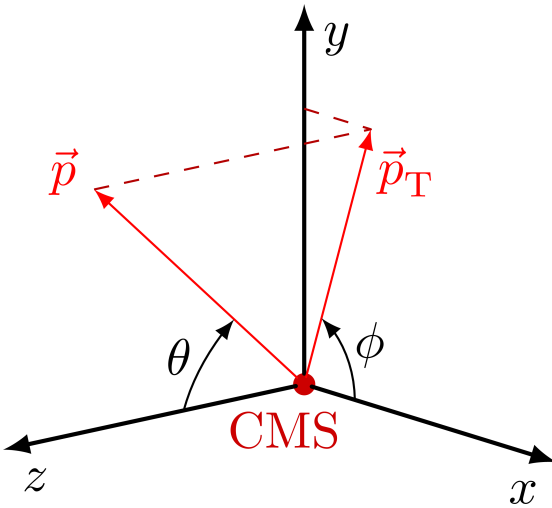


Figure 2.4: Coordinate system of the CMS. [21]

For high energy or massless particles, rapidity can be approximated by *pseudorapidity* (η).

$$\eta = -\ln \left(\tan \frac{\theta}{2} \right) \quad (2.5)$$

which only depends on the polar angle θ of the particle momentum. For $\eta = 0$ the particle moves perpendicular to the z -axis and for $\eta = \pm\infty$ is in $\pm z$ -direction. The distance between two particles is defined in the form of a Lorentz invariant ΔR variable:

$$\Delta R = \sqrt{\Delta\eta^2 + \Delta\phi^2} \quad (2.6)$$

2.2.2 The Superconducting Magnet

To detect particles ejected from the collision region, a superconducting solenoid magnet is employed to bend their trajectories. The CMS solenoid magnet, the largest of its kind ever constructed, provides sufficient space within its cylindrical frame to accommodate the Tracker, Electromagnetic Calorimeter, and Hadron Calorimeter systems, all arranged concentrically around the collision point. The magnet's NbTi superconducting coils carry currents of 18,500 Amps, generating magnetic fields up to 4 T. This high-strength magnetic field is confined within the detector by the steel return yoke, which constitutes the primary structural element of the detector, contributing approximately 12,500 tonnes of the total 14,000-tonne mass. To preserve the superconductivity of the coils, the system is maintained at cryogenic temperatures of 4.6 K using liquid helium.

2.2.3 Inner Tracker

The inner tracker of the CMS detector at CERN plays a pivotal role in detecting and reconstructing the trajectories of charged particles produced during high-energy proton-proton collisions at the LHC. Positioned at the innermost layers of the CMS, the tracker is integral to momentum measurement, vertex reconstruction, and particle identification, contributing significantly to a broad range of physics analyses.

Structural Design and Technology

The inner tracker is a cylindrical structure composed of multiple concentric layers of silicon sensors arranged around the beamline. The design incorporates the Pixel Detector at the core, surrounded by the Silicon Strip Tracker.

1. Pixel Detector

- Located closest to the collision point, the Pixel Detector is comprised of high-resolution silicon pixel sensors (approximately 100 μm by 150 μm in size).
- This configuration enables precise tracking of particles as they pass through the detector, capturing detailed information as close to the primary vertex as possible.

2. Silicon Strip Tracker

- Surrounding the Pixel Detector, the Silicon Strip Tracker consists of larger silicon strip sensors arranged across multiple barrel layers and extended by endcaps.
- These sensors provide extensive coverage for tracking particles beyond the inner layers, contributing to the overall detection of particle trajectories.

The tracker spans 5.8 meters in length and 2.5 meters in diameter, making it the first detector layer particles encounter after collision. The high granularity and fast response of the tracker are essential for handling the high collision rate at the LHC, with approximately 1000 particles produced from 20 overlapping interactions per bunch crossing every 25 ns.

Operational Principles

1. Charged Particle Detection

- As charged particles pass through the tracker, they ionize atoms in the silicon material, generating electric signals that are collected by the

applied electric field. Each interaction produces a measurable signal or “hit,” which is recorded at various points along the particle’s path.

- These hits, distributed across the layers, enable the reconstruction of the particle’s trajectory

2. Momentum and Charge Measurement

- The CMS solenoid magnet generates a 3.8 Tesla magnetic field that causes charged particles to follow curved paths. The degree of curvature is inversely proportional to the particle’s momentum; lower momentum results in more bending.
- By analyzing the curvature of the reconstructed tracks, the tracker provides both the charge and momentum of each particle.

3. Vertex Reconstruction

- The high spatial resolution of the tracker allows for precise identification of both primary vertices (collision points) and secondary vertices (decays of unstable particles).
- Tracking algorithms analyze the convergence of multiple tracks to distinguish between particles originating from the primary interaction and those resulting from secondary decays.

2.2.4 Energy Measurement

To study the interactions occurring during particle collisions, it is crucial to identify and measure the particles ejected into the detector, which requires precise energy and momentum measurements. The CMS detector utilizes specialized subsystems to detect different types of long-lived particles produced in these events, including electrons, photons, and hadrons.

The **Electromagnetic Calorimeter (ECAL)** is the subsystem responsible for detecting electrons and photons. Positioned just after the tracker, the ECAL is designed to fully absorb these particles, providing high-resolution measurements of their energy. When electrons or photons pass through the ECAL, they interact with the material, and the resulting energy deposition is measured to determine their energy with great precision. This makes the ECAL crucial for accurate electromagnetic energy measurements.

The **Hadron Calorimeter (HCAL)** surrounds the ECAL and is designed to detect and identify hadrons, such as protons, neutrons, and heavier nuclei. When

these particles pass through the tracker, they produce hadronic showers that are detected by the HCAL. The HCAL measures the energy of these heavy particles, providing critical information about hadronic interactions.

Together, the ECAL and HCAL provide comprehensive detection of both electromagnetic and hadronic components of the collision event, enabling precise reconstruction of particle energies. We will only focus on ECAL in this study which is presented in the section 2.3.

2.2.5 Muon System

Muons, as the heavier counterparts of electrons, are produced in high-energy collisions and are involved in various interesting decays, including the decay of the Z -boson, which is the focus of this study. Due to their higher penetrating power, muons are not fully absorbed by any of the CMS calorimeters. However, they leave a track in the inner tracker, which provides information for estimating their momentum. The primary energy deposition of muons occurs in the muon spectrometer, located outside the superconducting magnets and embedded within the iron yoke. This setup allows for a magnetic field of 1.8 Tesla to be utilized, enhancing the accuracy of muon p_T measurements. The muon spectrometer is composed of four types of gas chambers designed specifically for detecting these particles. Since the focus of this study is on electron (positron) signatures, further discussion of the muon spectrometer is not included, and attention will shift to the detailed analysis of the ECAL in the next section.

2.3 Electromagnetic Calorimeter

The electromagnetic calorimeter (ECAL) plays a critical role in studying electromagnetic objects like electrons (positrons) and photons. It is also valuable in measurements involving processes like Z boson decays, where the mass of the lepton pair can reveal details about the Z boson. The ECAL is composed of 61,200 lead tungstate ($PbWO_4$) crystals in the central barrel section, with an additional 7,324 crystals mounted in each endcap. The following are the main features of $PbWO_4$ crystals:

- The high density (8.28 g/cm^3), short radiation length X_0 (0.89 cm), and small Moliere radius (2.2 cm) results in a fine granularity and a compact calorimeter as limited by the magnet radius;
- Scintillation decay time is almost consistent with the nominal LHC bunch crossing rate; about 80% of the light is emitted in 25 ns.

- It is sufficiently radiation hard, allowing it to sustain several years of high luminosity running with tolerable degradation of the crystals' transparency, which can be corrected with a light monitoring system

The geometric crystal coverage extends up to $|\eta| = 3$. Precision energy measurements for photons and electrons will be performed within $|\eta| < 2.6$. The transverse granularity of $\Delta\eta \times \Delta\phi = 0.0175 \times 0.0175$, which corresponds to a crystal front face of approximately $22 \times 22 \text{ mm}^2$, closely aligns with the PbWO Molière radius of 21.9 mm. This small Molière radius minimizes the impact of pileup on energy measurements by reducing the area over which energy is accumulated. In the endcap region ($1.48 < |\eta| < 3.0$), granularity gradually increases, reaching a maximum of $\Delta\eta \times \Delta\phi \sim 0.05 \times 0.05$, though the size of the crystal front face remains constant. A thickness of around 26 radiation lengths at $|\eta| = 0$ is required to control the longitudinal shower leakage of high-energy electromagnetic showers within acceptable limits, translating to a crystal length of 23 cm in the barrel region.

2.3.1 Physics of the Electromagnetic Shower

Electrons and photons interact with matter primarily through quantum electrodynamics (QED) processes. For energies exceeding 10 MeV, the dominant mechanism of energy loss for electrons is *bremsstrahlung*, while photons in this energy range primarily lose energy through electron-positron pair production. At lower energies, electrons dissipate energy via ionization and thermal excitation, while photons primarily lose energy through Compton scattering and the photoelectric effect. High-energy electrons and photons ($\geq 1 \text{ GeV}$) create secondary particles: *bremsstrahlung* produces secondary photons, and pair production generates secondary electrons.

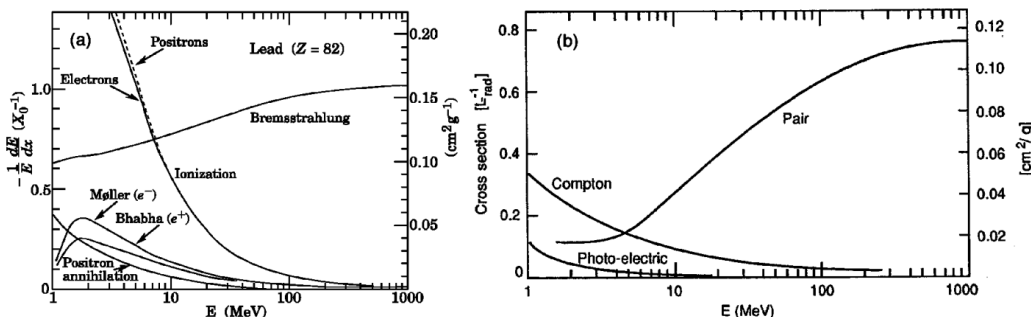


Figure 2.5: (a) Fractional energy lost in lead by electrons and positrons as a function of energy. (b) Photon interaction cross-section in lead as a function of energy.[22]

These secondary particles can initiate additional interactions, producing more

particles, though with progressively lower energy. This shower continues until the electron energy falls below a critical threshold, E_c , at which point energy dissipation occurs mainly through ionization and excitation.[23]

E_c can be defined in two ways:

- E_c , is the energy at which the electron ionization losses and *bremsstrahlung* losses become equal.

$$E_c = \frac{610(710) \text{ MeV}}{Z + 1.24(0.92)}, \quad \text{for solids(gases)} \quad (2.7)$$

- In the second definition (Rossi, 1952)[24], E_c is the energy at which the ionization loss per X_0 equals the electron energy E:

$$\frac{dE}{dx}(\text{ionization}) = \frac{E}{X_0} \quad (2.8)$$

Both definitions are equivalent in the approximation

$$\frac{dE}{dx}(\text{bremsstrahlung}) \simeq \frac{E}{X_0} \quad (2.9)$$

One of the main features of electromagnetic showers can be described in terms of one parameter, the radiation length X_0 ,[25] which depends on the characteristics of the material.

$$X_0(\text{g/cm}^2) \simeq \frac{716 \text{ g cm}^{-2} A}{Z(Z+1) \ln(287/\sqrt{Z})} \quad (2.10)$$

The radiation length governs the rate at which electrons lose energy by *bremsstrahlung*. It represents the average distance x that an electron needs to travel in material to reduce its energy to 1/e of its original energy, E_0 .

$$\langle E(x) \rangle = E_0 e^{-x/X_0} \quad (2.11)$$

Similarly for photons, the beam of initial intensity I_0 , is absorbed mainly through pair production. After traveling a distance $x = \frac{9}{7}X_0$, its intensity is reduced to 1/e of the original.

$$\langle I(x) \rangle = I_0 e^{-(7/9)(x/X_0)} \quad (2.12)$$

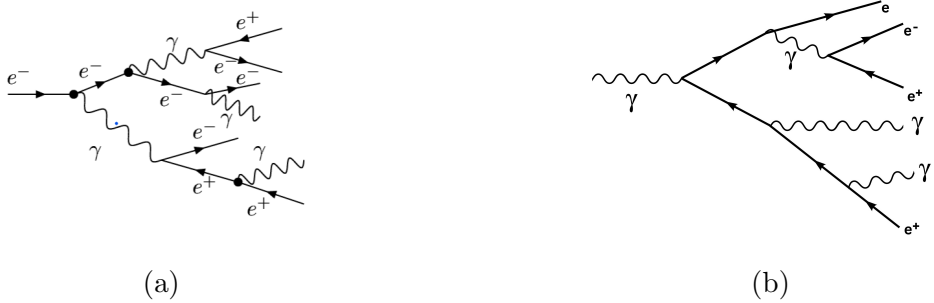


Figure 2.6: (a) and (b) show electron and photon showers respectively in the ECAL

2.3.2 Energy resolution of Electromagnetic Calorimeter

The measurement of energy with an ECAL is based on the principle that the energy released in the detector material by the charged particles is proportional to the incident energy of the incident particle. The track length of the shower T_0 , defined as the sum of all ionization tracks due to all charged particles in the shower is proportional to

$$T_0(g/cm^2) \propto X_0 \frac{E_0}{E_c} \quad (2.13)$$

where E_0/E_0 represents the number of particles in the shower.

The above formula shows that a measurement of the signal produced by the charged tracks of the shower provides a measurement of the original particle energy E_0 . This measurement can be performed, for instance, by detecting the light produced in a scintillating material, or by collecting the charge produced in a gas or a liquid.

The actual energy resolution of the calorimeter is determined by:

$$\left(\frac{\sigma}{E}\right)^2 = \left(\frac{S}{\sqrt{E}}\right)^2 + \left(\frac{N}{E}\right)^2 + C^2 \quad (2.14)$$

where,

- S is called the stochastic term or shower intrinsic fluctuations which represents the statistical error coming from electromagnetic shower evolution.
- N is the error in the energy measurement due to noise from the electronics and pile-up.
- C is a constant term related to the calibration of the calorimeter due to non-uniformity of light, inter-calibration error, and leakage of energy.

2.4 Electron Reconstruction and Identification

The reconstruction and identification of electrons are critical for distinguishing them from other particles, such as photons, muons, and hadrons. Electrons deposit energy in the Electromagnetic Calorimeter (ECAL) and leave tracks in the tracker, providing key signatures for their detection.

Reconstruction involves associating energy deposits in the ECAL with the corresponding tracks in the inner tracker, enabling the detection of electron candidates. The identification then distinguishes the true electrons from the other particles using criteria based on the shape of the shower, the matching of the track cluster and the isolation variables. These steps are essential for isolating signal electrons from background, ensuring high efficiency and purity in the analysis.

2.4.1 Electron Clustering and Superclustering

Energy deposits in ECAL crystals are initially grouped into clusters, with the cluster containing the highest energy deposit in a given region identified as the seed cluster. A seed cluster is required to have a transverse energy (E_T^{seed}) exceeding 1 GeV. Electrons and photons typically deposit their energy across multiple crystals. Under ideal conditions, with no material in front of the calorimeter, approximately 97% of the energy of a single electron or photon is contained within a crystal array 5×5 . However, in a realistic detector environment, material interactions in front of the ECAL result in energy dispersion. Electrons radiate energy via bremsstrahlung in the tracker, while photons convert into electron-positron pairs, causing their energy to spread over a larger area. Consequently, energy deposits become distributed along the ϕ -direction, which fixed crystal arrays are unable to fully capture.

To address this, the reconstruction algorithm combines clusters into superclusters, which account for energy dispersion due to bremsstrahlung and photon conversions. This strategy ensures a more complete recovery of the total energy. For electrons, reconstruction begins by identifying seed clusters from the highest-energy crystals in the ECAL. These seed clusters are then expanded into superclusters to include energy radiated during bremsstrahlung, thereby improving energy resolution.[26]

2.4.2 Track Reconstruction

Electron track reconstruction involves identifying and measuring the path an electron takes through the detector using hits from the silicon tracker. The process starts by finding seeds—patterns of hits in tracker layers—that are typically chosen near energy deposits in the ECAL, connecting the track to the electron’s

energy. The reconstruction algorithm then links these seeds across the tracker layers, forming a continuous path. Due to energy loss from bremsstrahlung radiation, the electron's path may have irregularities, which the algorithm accounts for. The track is refined through a fitting process that adjusts for these energy losses. Finally, the reconstructed track is matched with energy clusters in the ECAL to ensure it corresponds to the same electron. This process provides precise information on the trajectory, momentum and direction of the electron, which is essential for further analysis.

2.4.3 Electron Identification

Electron identification is the process of distinguishing electrons from other particles, such as photons, muons, or hadrons, in a particle detector. Electron identification makes use of a complete set of variables to distinguish between real electrons and background electrons.

These variables are:

- H/E: Hadronic to electromagnetic energy ratio. A ‘good’ electron will show little to no hadronic energy deposit, as the electron deposits significant energy in the electromagnetic calorimeter. For a ‘good’ electron, $H/E < 0.15$.
- $E_{ECAL}/p_{track} \approx 1$, The energy deposited in the ECAL should be consistent with the momentum measured on the track.
- $\Delta\phi_{in}$, $\Delta\eta_{in}$, geometrical matching between the electron track parameters at the vertex extrapolated to the super-cluster and the measured super-cluster position. For a ‘good’ electron they should be small.
- $|\frac{1}{E} - \frac{1}{p}|$, Energy-momentum matching variable where E is the Supercluster energy and P is the track momentum at the point of closest approach to the vertex.
- Missing hits: Numbers of tracker layers crossed by the reconstructed electron track without a corresponding hit in the recorded in that layer.
- d_y : Transverse impact parameter of the electron track with respect to the reconstructed primary vertex.
- d_z : Longitudinal impact parameter of the electron track with respect to the reconstructed primary vertex.

Chapter 3

Data Analysis

3.1 Data Acquisition

The data utilized in this analysis is sourced from the *CERN Open Data Portal*[27]. The signal Monte Carlo (MC) sample corresponds to the **DYJetsToLL_M-50-LO** process, which simulates Drell-Yan (DY) production of lepton-antilepton pairs ($\ell^+\ell^-$) with an invariant mass greater than 50 GeV. This is the primary signal of interest in the study.

The Background Monte Carlo samples include the following processes:

1. TTTTo2L2Nu: Simulates $t\bar{t}$ production with both tops decaying leptonically, producing two leptons and two neutrinos in the final state:

$$t\bar{t} \rightarrow (bW^+)(\bar{b}W^-) \rightarrow (b\ell^+\nu_\ell)(\bar{b}\ell'^-\bar{\nu}_{\ell'}).$$

2. WWTo2L2Nu: Simulates the production of a pair of W -bosons, both decaying leptonically, resulting in two leptons and two neutrinos:

$$W^+W^- \rightarrow (\ell^+\nu_\ell)(\ell'^-\bar{\nu}_{\ell'}).$$

3. WZTo3LNu: Describes the production of a W -boson and a Z -boson, where the W -boson decays leptonically and the Z -boson decays into a pair of leptons:

$$W^\pm Z \rightarrow (\ell^+\nu_\ell)(\ell'^+\ell'^-).$$

4. ZZTo4L: Simulates the production of a pair of Z -bosons, each decaying leptonically into a pair of leptons:

$$ZZ \rightarrow (\ell^+\ell^-)(\ell'^+\ell'^-).$$

5. TTSemileptonic: Simulates top quark-antiquark ($t\bar{t}$) production where one top quark decays semileptonically:

$$t\bar{t} \rightarrow (bW^+)(\bar{b}W^-) \rightarrow (b\ell^+\nu_\ell)(\bar{b}q\bar{q}').$$

Several background processes can mimic the $q\bar{q} \rightarrow Z \rightarrow e^+e^-$ signal. Semileptonic $t\bar{t}$ decays (`TTSemileptonic`) can fake the signal when jets from hadronic decays are misidentified as electrons, producing e^+e^- pairs accompanied by jets. Fully leptonic $t\bar{t}$ decays (`TTTo2L2Nu`) can directly produce e^+e^- pairs, but these events often include b -jets. Di-boson processes, such as $WW \rightarrow 2\ell 2\nu$, generate two real leptons, including e^+e^- , with E_T^{miss} from neutrinos. In $WZ \rightarrow 3\ell\nu$, if one lepton is undetected, the event can appear as e^+e^- with missing energy. For $ZZ \rightarrow 4\ell$, the background arises when two leptons are outside the detector acceptance, misidentified, or not reconstructed, leaving an apparent e^+e^- pair. Additionally, if one Z -boson decays to e^+e^- with an invariant mass near the Z -boson mass, it becomes challenging to distinguish from the signal. These backgrounds necessitate careful event selection using lepton isolation, jet vetoes, E_T^{miss} thresholds, and invariant mass cuts to enhance the signal-to-background ratio. To suppress these backgrounds, several strategies are employed. Events with significant E_T^{miss} or additional jets are rejected to reduce contributions from $t\bar{t}$ and WW processes. Lepton isolation criteria are applied to distinguish real electrons from misidentified jets. Additionally, an invariant mass cut is used to select e^+e^- pairs within the Z -boson mass window ($m_{e^+e^-} \approx 91$ GeV), which suppresses contributions from non-resonant backgrounds. These techniques are essential for enhancing the purity of the $q\bar{q} \rightarrow Z \rightarrow e^+e^-$ signal.

3.2 Selection Criteria

The selection criteria for di-lepton events are designed to isolate high-quality, physically meaningful data while suppressing background processes. These criteria focus on events involving two leptons in the final state, particularly targeting processes such as Z -boson decays into an electron-positron pair. The conditions applied ensure both experimental feasibility and physical significance.

The full set of cuts is summarized in Table 3.1.

First, the events must contain exactly two leptons. This condition narrows the analysis to di-lepton final states, simplifying event reconstruction and focusing on processes where two leptons are expected. To ensure the leptons are energetic and detectable, a minimum transverse momentum threshold is imposed, requiring the leading lepton to have a transverse momentum above 25 GeV and the subleading lepton above 20 GeV. These thresholds help eliminate contributions from low-energy background processes.

To further constrain the leptons' detectability, their pseudorapidity is restricted to within the detector's acceptance region, specifically $|\eta| < 2.5$. This ensures the leptons are well within the range where the detector operates most efficiently.

Criterion	Description
Lepton Multiplicity	Exactly two leptons in the event
Transverse Momentum (p_T)	Leading lepton: $p_T > 25$ GeV, Subleading lepton: $p_T > 20$ GeV
Pseudorapidity ($ \eta $)	Both leptons must satisfy $ \eta < 2.5$
Lepton Pair Charge	Oppositely charged lepton pair (e^+e^-)
Invariant Mass ($m_{\ell\ell}$)	60 GeV $< m_{\ell\ell} < 120$ GeV
Electron Identification	Both leptons must pass ‘Tight’ electron ID (MVA Fall17V2Iso WP90)

Table 3.1: Summary of selection criteria for di-lepton events.

To identify the type of lepton pair, the selection ensures that the two leptons are an oppositely charged electron and positron. This is achieved by constraining the particle ID to match the expected behavior of an electron-positron pair, as produced in processes like Z -boson decays.

The invariant mass of the lepton pair is then required to fall within the range of 60–120 GeV. This window encompasses the mass of the Z -boson (91.2 GeV) and excludes contributions from low-mass resonances or high-mass backgrounds. This range ensures the selection is enriched with events consistent with Z -boson decays.

Finally, a stringent identification criterion is applied to the leptons. Both leptons must pass the ‘Tight’ electron identification requirements, as defined by a multivariate analysis working point. This ensures the selected leptons are genuine electrons and minimizes contamination from misidentified particles, such as jets or hadrons.

3.3 Drell-Yan ($Z \rightarrow e^+e^-$) Plots

In this section, we will present several plots that illustrate the behavior of our signal within the ‘cutted’ region defined in the previous section. First, we will examine how quantities such as p_T , η differ for the leading and trailing leptons, specifically focusing on electrons in our case. Following that, we will plot the invariant mass of the di-electron system, the transverse momentum between the di-electron pair, the azimuthal angle difference between the two electrons, and the missing transverse energy.

Here are the definition of invariant mass, transverse momentum, and azimuthal angle difference of di-electron.

- **Invariant mass of di-electron**

The invariant mass of a di-electron system is calculated using the four-momentum of the two electrons.

$$M_{\ell\ell} = \sqrt{(E_1 + E_2)^2 - (\vec{p}_1 + \vec{p}_2)^2} \quad (3.1)$$

where:

- $m_{\ell\ell}$ is the invariant mass of the di-electron system.
- E_1 and E_2 are the energies of the two electrons.
- \vec{p}_1 and \vec{p}_2 are the three-momenta of the two electrons.

- **Transverse momentum of di-electron**

The transverse momentum of the di-electron system, denoted as $p_{T\ell\ell}$, is given by:

$$p_{T\ell\ell} = \sqrt{(p_x^1 + p_x^2)^2 + (p_y^1 + p_y^2)^2} \quad (3.2)$$

where, p_x^i and p_y^i are the momentum of leptons in x and y directions.

- **Azimuthal angle difference** The azimuthal angle difference of the di-electron system, denoted as $\Delta\phi_{\ell\ell}$, is given by:

$$\Delta\phi_{\ell\ell} = |\phi_1 - \phi_2| \quad (3.3)$$

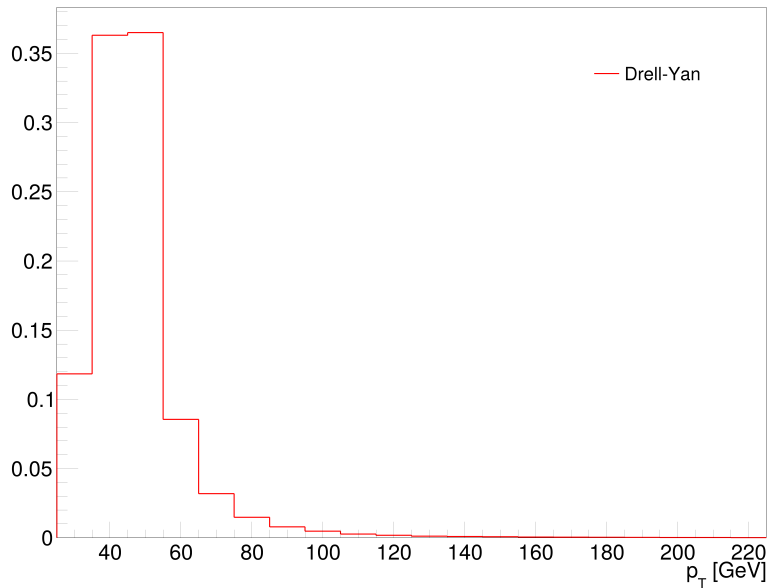
where:

- ϕ_1 and ϕ_2 are the azimuthal angles of the two electrons in the transverse plane, defined as:

$$\phi_1 = \tan^{-1} \left(\frac{p_{y1}}{p_{x1}} \right), \quad \phi_2 = \tan^{-1} \left(\frac{p_{y2}}{p_{x2}} \right) \quad (3.4)$$

CMS

Leading Lepton pT

(a) p_T of leading electron

CMS

Trailing Lepton pT

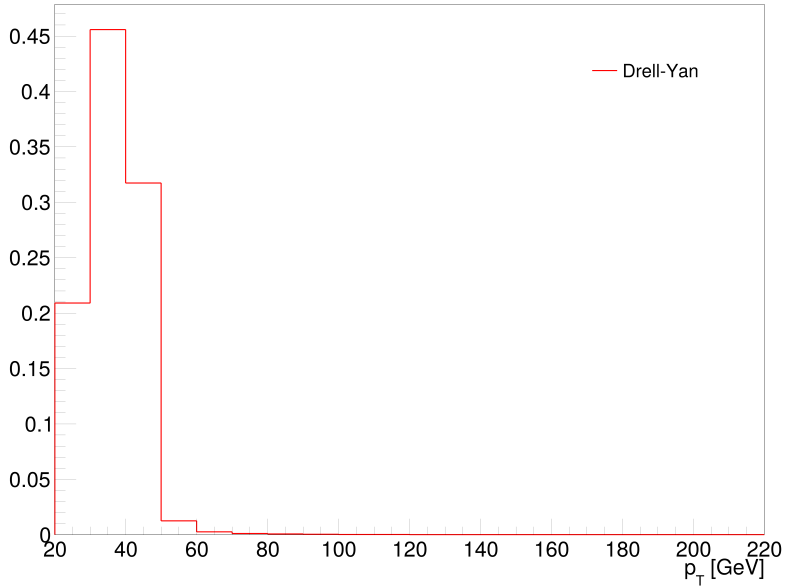
(b) p_T of leading electron.

Figure 3.1: Transverse momentum of leading and trailing electron after passing the selection cuts.

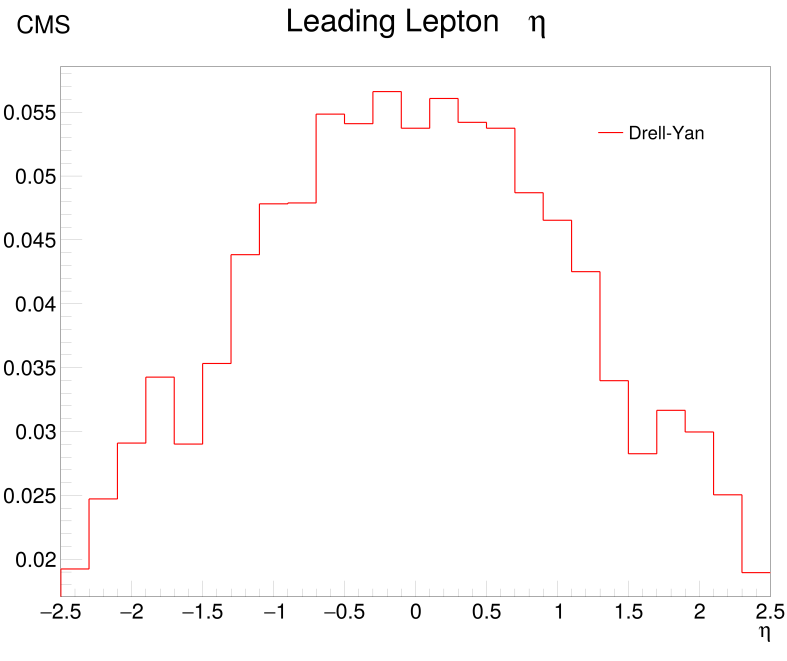
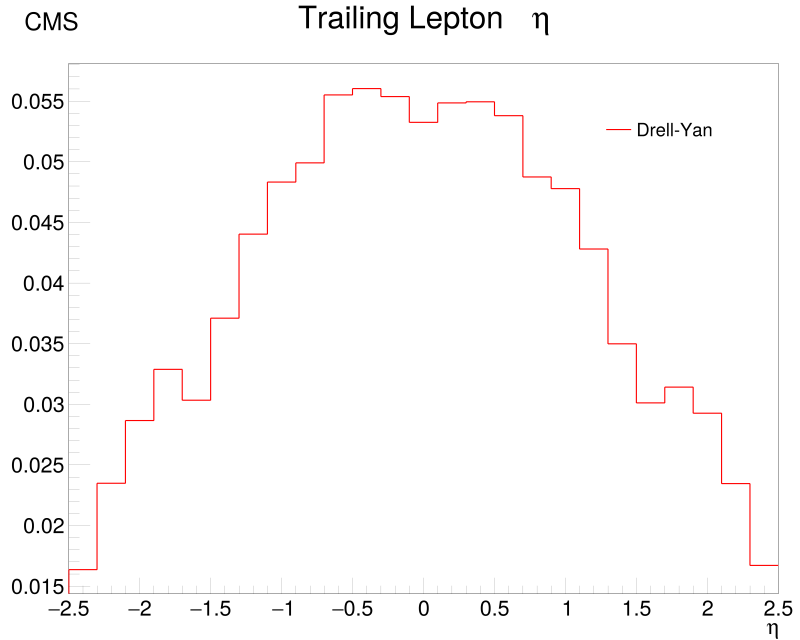
(a) η of leading electron(b) η of leading electron.

Figure 3.2: Pseudorapidity of leading and trailing electron after passing the selection cuts.

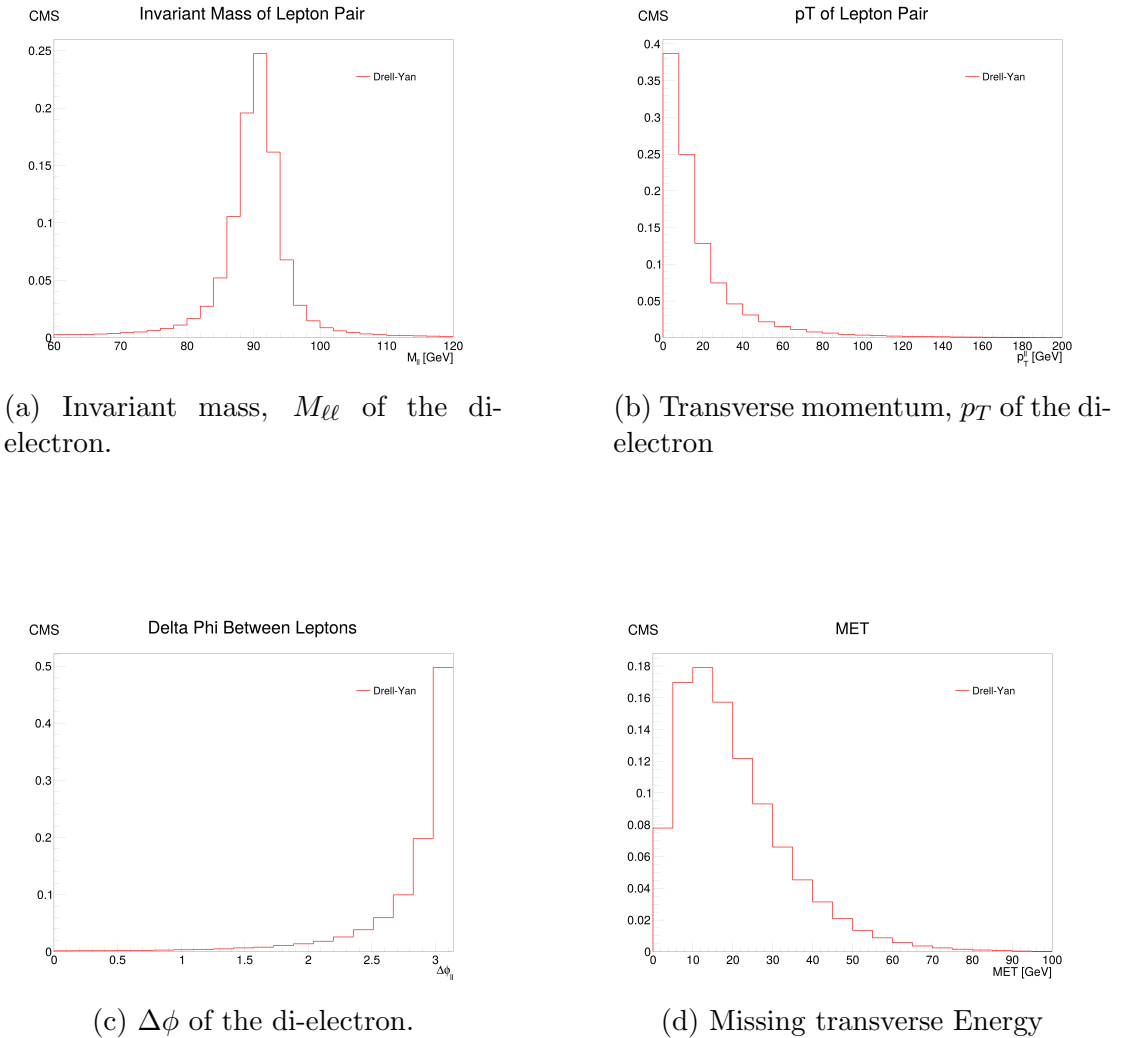
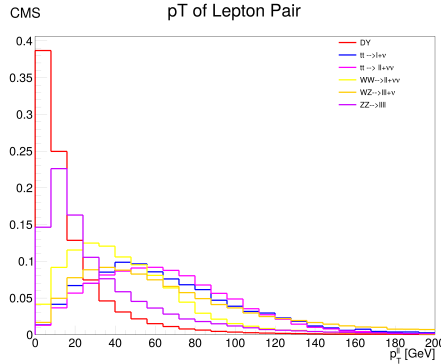


Figure 3.3: Plots for the $M_{\ell\ell}$, $p_{T\ell\ell}$, $\Delta\phi_{\ell\ell}$, and Missing transverse energy for the Drell-Yan signal. The calculation of these quantities are shown above.

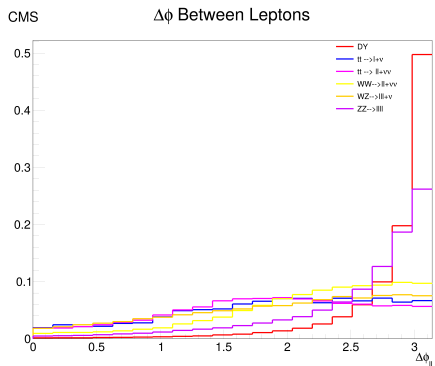
From the $M_{\ell\ell}$ plot, it is evident that the mass distribution is centered around 90 GeV, corresponding to the Z boson's predicted mass. The next section will examine how background processes can cause deviations in these quantities from the expected behavior.

3.4 Plots with Backgrounds

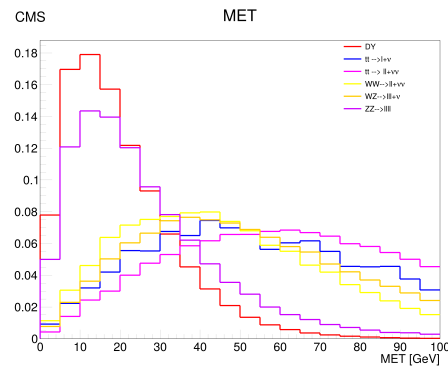
In the following, we will explore how the background processes discussed in section 3.1 may lead to deviations in the results from the expected values. A summary of the backgrounds considered can be found in section 3.1.



(a) Transverse momentum, p_T of the lepton pair with backgrounds

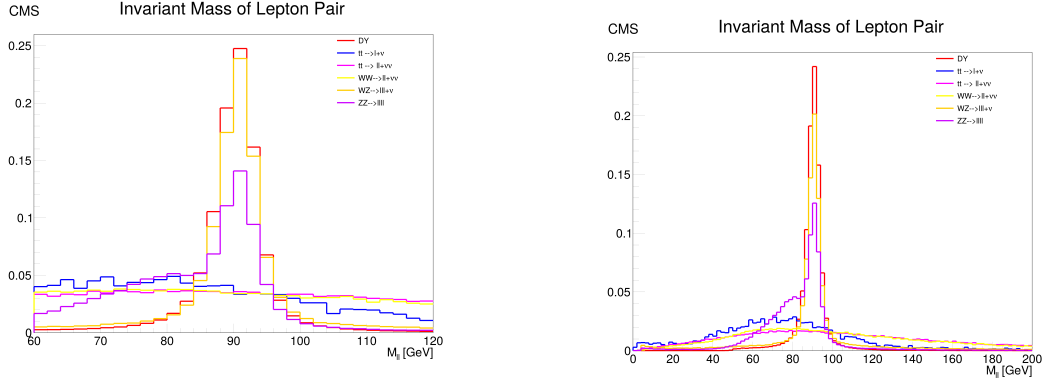


(b) $\Delta\phi$ between leptons with backgrounds



(c) Missing transverse Energy with backgrounds

Figure 3.4: Plots for the $p_{T\ell\ell}$, $\Delta\phi_{\ell\ell}$, and Missing transverse energy for the Drell-Yan signal along with the pre-mentioned backgrounds. This analysis is based on setting a cut on invariant mass, $60 < M_{\ell\ell} < 120$.



(a) Invariant mass, $M_{\ell\ell}$ of the lepton pair with cuts $60 \text{ GeV} < M_{\ell\ell} < 120 \text{ GeV}$.

(b) Invariant mass, $M_{\ell\ell}$ of the lepton pair without cuts.

Figure 3.5: Comparison of invariant mass, $M_{\ell\ell}$, of the lepton pair with (left) and without (right) cuts applied.

Figure 3.5a illustrates the data after applying $M_{\ell\ell}$ cuts, whereas Figure 3.5b presents the data without any such cuts. A clear reduction in background dominance is observed in the intermediate-mass region (60–120 GeV) when the $M_{\ell\ell}$ cuts are applied. This highlights the effectiveness of mass-based selection criteria in suppressing background contributions. Motivated by these findings, we will focus on developing techniques and algorithms in the next semester to further enhance background suppression and improve signal extraction efficiency.

Chapter 4

Conclusion

In this study, we explored the interaction of various radiations with matter to understand the behavior of our signature (electron) and how it aids in identification. A qualitative overview of the Drell-Yan process was presented, emphasizing its significance without delving into extensive theoretical details. We then examined the LHC and the CMS experiment, focusing on how the CMS detector measures the energy of electrons and facilitates their reconstruction and identification.

Using MC simulation data, we analyzed the signatures of the Drell-Yan process ($Z \rightarrow e^+e^-$), studying key observables such as invariant mass, transverse momentum, and azimuthal angle differences of the di-electron. Along with the pseudorapidity (η), transverse momentum (p_T), and azimuthal angle (ϕ) of leading and trailing electrons. These results were complemented by an examination of how various background processes can introduce deviations from the expected distributions.

In the next semester, the focus will shift to developing and implementing techniques and algorithms to suppress background interference further and enhance the extraction of the desired signal.

Bibliography

- [1] Hans Bichsel and Heinrich Schindler. *The Interaction of Radiation with Matter*, page 5. 09 2020.
- [2] Glenn F. Knoll. *Radiation Detection and Measurement, 3rd edition*, pages 29,30. John Wiley and Sons, New York, 2000.
- [3] Glenn F. Knoll. *Radiation Detection and Measurement, 3rd edition*, page 31. John Wiley and Sons, New York, 2000.
- [4] S. Navas et al. Review of particle physics. *Phys. Rev. D*, 110(3):030001, 2024.
- [5] Glenn F. Knoll. *Radiation Detection and Measurement*, page 42. John Wiley and Sons, New York, 3rd edition edition, 2000.
- [6] J. D. Jackson. *Classical Electrodynamics*, page 509. Wiley, New York, 1962.
- [7] Massachusetts Institute of Technology. Applied nuclear physics, lecture 15: Bremsstrahlung, 2006. Accessed: 2024-11-14.
- [8] Glenn F. Knoll. *Radiation Detection and Measurement*, page 43. John Wiley and Sons, New York, 3rd edition edition, 2000.
- [9] Hans Bichsel and Heinrich Schindler. *The Interaction of Radiation with Matter*, pages 6–7. 09 2020.
- [10] M. J. Berger et al. XCOM: Photon cross sections database. <https://www.nist.gov/pml/xcom-photon-cross-sections-database>. Accessed: 2024-11-19.
- [11] Sidney D. Drell and Tung-Mow Yan. Massive lepton-pair production in hadron-hadron collisions at high energies. *Phys. Rev. Lett.*, 25:316–320, Aug 1970.
- [12] G. Arnison et al. Experimental Observation of Lepton Pairs of Invariant Mass Around $95 \text{ GeV}/c^2$ at the CERN SPS Collider. *Phys. Lett. B*, 126:398–410, 1983.

- [13] K. Nakamura et al. Review of particle physics. *J. Phys. G*, 37:075021, 2010.
- [14] Lyndon Evans and Philip Bryant. Lhc machine. *Journal of Instrumentation*, 3(08):S08001, aug 2008.
- [15] R. P. Walker. Synchrotron radiation. Technical report, CERN, 1994.
- [16] Energy Blog at UCI. Introduction to the large hadron collider at cern, 2012. Accessed: 2024-11-16.
- [17] G. L. Bayatian et al. CMS Physics: Technical Design Report Volume 1: Detector Performance and Software, 2006.
- [18] CMS Open Data Workshop. Cms detector - overview, 2024. Accessed: 2024-11-17.
- [19] CMS Open Data Workshop. Cms detector - images and graphics, 2024. Accessed: 2024-11-17.
- [20] Arun Kumar. *Search for the Standard Model Higgs Boson in the $H \rightarrow ZZ \rightarrow ee(\mu\mu\mu\mu) \nu\nu$ channel in the CMS Experiment at LHC*. PhD thesis, UNIVERSITY OF DELHI, 2014.
- [21] TikZ.net. 3d cms detector axis example with tikz, 2024. Accessed: 2024-11-17.
- [22] Christian W. Fabjan and Fabiola Gianotti. Calorimetry for particle physics, 2003. Published 15 October 2003.
- [23] Christian W. Fabjan and Fabiola Gianotti. Calorimetry for particle physics. *Reviews of Modern Physics*, 82(3):2391–2452, 2010.
- [24] B. Rossi. *High Energy Particles*. Prentice Hall, Englewood Cliffs, NJ, 1952.
- [25] K. Nakamura et al. Review of particle physics. *J. Phys. G*, 37:291, 2010.
- [26] Sirunyan et al. Electron and photon reconstruction and identification with the cms experiment at the cern lhc. *Journal of Instrumentation*, 16:5, 2021.
- [27] CERN. Cms open data. <https://opendata.cern.ch/search?q=&f=experiment%3ACMS&l=list&order=desc&p=1&s=10&sort=mostrecent>. Accessed: 2024-11-25.